Searching for Heavier Higgs Boson via Di-Higgs Production at LHC Run-2

Lan-Chun Lü [*] [a], Chun Du [†] [b], Yaquan Fang [‡] [b], Hong-Jian He [§] [a,c,d], Huijun Zhang [¶] [e]

[a] Institute of Modern Physics and Center for High Energy Physics, Tsinghua University, Beijing 100084, China
[b] Institute of High Energy Physics, Beijing 100049, China
[c] Institute for Advanced Study, Princeton, NJ 08540, USA
[d] Harvard University, 1 Oxford Street, Cambridge, MA 02138, USA
[e] Nanjing University, Nanjing 210093, China

Abstract

The LHC discovery of a light Higgs particle $h^0\,(125\,\mathrm{GeV})$ opens up new prospect for searching heavier Higgs boson(s) at the LHC Run-2, which will unambiguously point to new physics beyond the standard model (SM). We study the detection of a heavier neutral Higgs boson H^0 via di-Higgs production channel at the LHC (14 TeV), $H^0 \to h^0 h^0 \to WW^*\gamma\gamma$. This directly probes the Hhh cubic Higgs interaction, which exists in most extensions of the SM Higgs sector. For the decay products of final states WW^*, we include both pure leptonic mode $WW^* \to \ell\bar{\nu}\bar{\ell}\nu$ and semi-leptonic mode $WW^* \to q\bar{q}'\ell\nu$. We analyze signals and backgrounds by performing fast detector simulation for the full processes $pp \to H \to hh \to WW^*\gamma\gamma \to \ell\bar{\nu}\bar{\ell}\nu\gamma\gamma$ and $pp \to H \to hh \to WW^*\gamma\gamma \to \ell\nu q\bar{q}'\gamma\gamma$, over the mass range $M_H = 250 - 600\,\mathrm{GeV}$. For generic two-Higgs-doublet models (2HDM), we present the discovery reach of the heavier Higgs boson at the LHC Run-2, in comparison with the current Higgs global fit of the 2HDM parameter space.

Keywords: LHC, New Higgs Boson, Beyond Standard Model Searches

PACS numbers: 12.15.Ji, 12.60.-i, 12.60.Fr, 14.80.Ec [arXiv:1507.02644]

1. Introduction

Most extensions of the standard model (SM) require an enlarged Higgs sector, containing more than one neutral Higgs states. After the LHC discovery of a light Higgs particle $h^0\,(125\,\mathrm{GeV})$ [1][2], a pressing task of the on-going LHC Run-2 is to search for additional new Higgs boson(s), which will unambiguously point to new physics beyond the SM.

Such an enlarged Higgs sector [3] may contain additional Higgs doublet(s), or Higgs triplet(s), or Higgs singlet(s). For instance, the minimal supersymmetric SM (MSSM) [4] always requires two Higgs doublets and its next-to-minimal extension (NMSSM) [5] further adds a Higgs singlet. The minimal gauge extensions with extra SU(2) or U(1) gauge group [6][7] will invoke an additional Higgs doublet or singlet. The minimal left-right symmetric models [8] include an extra product group $\mathrm{SU}(2)_R \otimes \mathrm{U}(1)_{B-L}$, and thus requires a Higgs bidoublet plus two Higgs triplets. For the demonstration in our present LHC study, we will consider generic two-Higgs-doublet models (2HDM) [9] under the SM gauge group. To evade constraints of flavor changing neutral current (FCNC), it is common to impose a discrete $\mathbb{Z}_2$ symmetry on the 2HDM. For different model settings of Higgs Yukawa interactions, the 2HDMs are conventionally classified into type-I, type-II, lepton-specific, neutrino-specific, and flipped 2HDMs [9]. The current study will focus on the conventional type-I and type-II 2HDMs.

For the heavier Higgs state H^0 with mass above twice of the light Higgs boson h^0, $M_H > 2M_h \simeq 250\,\mathrm{GeV}$, the di-Higgs decay channel $H \to hh$ is opened and becomes significant, in addition to the other SM-like major decay modes $H \to WW, ZZ$. Hence, the LHC can search for the di-Higgs production channel $pp \to H \to hh$ [4, 6, 10, 11]. ATLAS analyzed the decay channel $hh \to b\bar{b}\gamma\gamma$ at the LHC (8 TeV) run and found a 2.4σ excess at $M(b\bar{b}\gamma\gamma) \simeq 300\,\mathrm{GeV}$ [12]. CMS performed similar searches for this channel and derived limits on the parameter space [13]. An analysis of this channel at 14 TeV runs with high luminosity $1000\,\mathrm{fb}^{-1}$ was done for 2HDM [14]. Another study considered the SM plus a heavy singlet scalar via $H \to hh \to b\bar{b}WW^* \to b\bar{b}\ell\nu\ell\nu$ channel for 14 TeV runs with $3000\mathrm{fb}^{-1}$ luminosity [15]. We note that it is possible to increase the sensitivity of H^0 searches by studying and combining more decay channels of the di-Higgs bosons.

[*] lvlc10@mails.tsinghua.edu.cn
[†] chun.thazen.du@gmail.com
[‡] fangyq@ihep.ac.cn (corresponding author)
[§] hjhe@tsinghua.edu.cn (corresponding author)
[¶] huijun.zhang@cern.ch

In this work, we perform systematical study of H^0 production via a new decay channel of di-Higgs bosons, $pp \to H \to hh \to WW^*\gamma\gamma$, where we consider pure leptonic mode $WW^* \to \ell\bar{\nu}\bar{\ell}\nu$ and semi-leptonic mode $WW^* \to q\bar{q}'\ell\nu$. Since a SM-like Higgs boson h^0 (125 GeV) has decay branching fractions $\mathrm{Br}[h \to b\bar{b}, WW^*, ZZ^*] \simeq (58\%, 22.5\%, 2.77\%)$, we see that the di-Higgs decay mode $hh \to WW^*\gamma\gamma$ (with pure leptonic or semi-leptonic WW^* decays) has the advantage of much cleaner backgrounds than $hh \to b\bar{b}\gamma\gamma$, while $\mathrm{Br}[h \to WW^*]$ is only smaller than $\mathrm{Br}[h \to b\bar{b}]$ by a factor of about 2.6. Hence, we expect that the $hh \to WW^*\gamma\gamma$ mode should have comparable sensitivity to $hh \to b\bar{b}\gamma\gamma$ mode, and is more sensitive than $hh \to b\bar{b}WW^*$ mode.

This paper is organized as follows. In Sec. 2, we present the production and decays of the heavier Higgs boson H^0 in the 2HDM of type-I and type-II. Then, in Sec. 3 we systematically analyze the signals and backgrounds for the reaction $pp \to H \to hh \to WW^*\gamma\gamma$, including both pure leptonic and semi-leptonic decay modes of the WW^* final state. In Sec. 4, we further analyze the LHC probe of the parameter space for 2HDM-I and 2HDM-II. Finally, we conclude in Sec. 5.

2. Decays and Production of Heavier Higgs Boson H^0 in the 2HDM

2.1. 2HDM Setup and Parameter Space

For the present phenomenological study, we consider the 2HDM [9] as the minimal extension of the SM Higgs sector. We set the Higgs potential to have CP conservation, and the two Higgs doublets $\mathbb{H}_1$ and $\mathbb{H}_2$ have hypercharge $Y = +\frac{1}{2}$, under the convention $Q = I_3 + Y$. It is desirable to assign a discrete $\mathbb{Z}_2$ symmetry to the Higgs sector, under which the Higgs doublet $\mathbb{H}_1$ ($\mathbb{H}_2$) is $\mathbb{Z}_2$ even (odd). With these, the Higgs potential can be written as

$$\begin{aligned} V &= M_{11}^2|\mathbb{H}_1|^2 + M_{22}^2|\mathbb{H}_2|^2 - M_{12}^2(\mathbb{H}_1^\dagger\mathbb{H}_2 + \mathbb{H}_2^\dagger\mathbb{H}_1) + \frac{\lambda_1}{2}(\mathbb{H}_1^\dagger\mathbb{H}_1)^2 + \frac{\lambda_2}{2}(\mathbb{H}_2^\dagger\mathbb{H}_2)^2 \\ &\quad + \lambda_3|\mathbb{H}_1|^2|\mathbb{H}_2|^2 + \lambda_4|\mathbb{H}_1^\dagger\mathbb{H}_2|^2 + \frac{\lambda_5}{2}\Big[(\mathbb{H}_1^\dagger\mathbb{H}_2)^2 + (\mathbb{H}_2^\dagger\mathbb{H}_1)^2\Big], \end{aligned} \tag{1}$$

where the masses and couplings are real, and we have allowed a soft $\mathbb{Z}_2$ breaking mass term of M_{12}^2. The minimization of this Higgs potential gives the vacuum expectation values (VEVs), $\langle\mathbb{H}_1\rangle = \frac{1}{\sqrt{2}}(0,\, v_1)^T$ and $\langle\mathbb{H}_2\rangle = \frac{1}{\sqrt{2}}(0,\, v_2)^T$. The two doublets jointly generate the electroweak symmetry breaking (EWSB) VEV $v \simeq 246\,\mathrm{GeV}$, via the relation $v = (v_1^2 + v_2^2)^{1/2}$, where $v_1 = v\cos\beta$ and $v_2 = v\sin\beta$. Thus, the parameter $\tan\beta$ is determined by the Higgs VEV ratio, $\tan\beta = v_2/v_1$. The two Higgs doublets contain eight real components in total,

$$\mathbb{H}_j = \begin{pmatrix} \pi_j^+ \\ \frac{1}{\sqrt{2}}\left(v_j + h_j + i\pi_j^0\right) \end{pmatrix}, \qquad (j = 1, 2). \tag{2}$$

Three imaginary components are absorbed by $(W^\pm,\, Z^0)$ gauge bosons, while the remaining five components give rise to the two CP-even neutral states $(h_1^0,\, h_2^0)$, one CP-odd neutral state A^0, and two charged states $H^\pm$. The mass eigenstates $(h,\, H)$ of the neutral CP-even Higgs bosons are given by diagonalizing the mass terms in the Higgs potential (1). They are mixtures of the gauge eigenstates $(h_1,\, h_2)$,

$$\begin{pmatrix} h \\ H \end{pmatrix} = \begin{pmatrix} \cos\alpha & -\sin\alpha \\ \sin\alpha & \cos\alpha \end{pmatrix}\begin{pmatrix} h_2 \\ h_1 \end{pmatrix}, \tag{3}$$

where α is the mixing angle. Among the two neutral Higgs bosons, h is the SM-like Higgs boson with mass $M_h \simeq 125\,\mathrm{GeV}$, as discovered at the LHC Run-1 [1][2], and H is the heavier Higgs state. We will systematically study the LHC discovery potential of H state in the present work. The Higgs potential (1) contains 8 parameters in total, three masses and five couplings. Among these, we redefine 7 parameters as follows: the EWSB VEV v, the VEV ratio $\tan\beta$, the mixing angle α, and the mass-eigenvalues $(M_h, M_H, M_A, M_{H^\pm})$. We may choose the 8th parameter as the Higgs mass-parameter M_{12}^2. Note that once we fix the mass spectrum of the 5 Higgs bosons as inputs, we are left with only 3 independent parameters $(\alpha\,, \tan\beta)$ and M_{12}^2. The current LHC data favor the parameter space of the 2HDM around the alignment limit [9], under which $\cos(\beta - \alpha) = 0$. This limit corresponds to the light Higgs state h to behave as the SM Higgs boson with mass 125 GeV. For practical analysis, we fix $M_h \simeq 125\,\mathrm{GeV}$ by the LHC data and vary the heavier mass M_H within the range of $250 - 600\,\mathrm{GeV}$. We consider the Higgs states A and $H^\pm$ to be relatively heavy, within the mass-range $M_A, M_{H^\pm} = 0.3 - 2\,\mathrm{TeV}$ for simplicity. We will scan the parameter space and analyze the LHC production and decays of H in the next section.

The heavier neutral Higgs boson H has gauge couplings with $(W^\pm,\, Z^0)$ and Yukawa couplings with quarks and leptons, which depend on the VEV ratio $\tan\beta$ and mixing angle α. The gauge couplings of H with $V\,(= W, Z)$ differ from the SM Higgs coupling by a scaling factor $\cos(\beta-\alpha)$,

$$G_{HVV} = \cos(\beta-\alpha)\, G_{HVV}^{\mathrm{sm}}, \qquad G_{HVV}^{\mathrm{sm}} = \frac{2M_V^2}{v}. \tag{4}$$

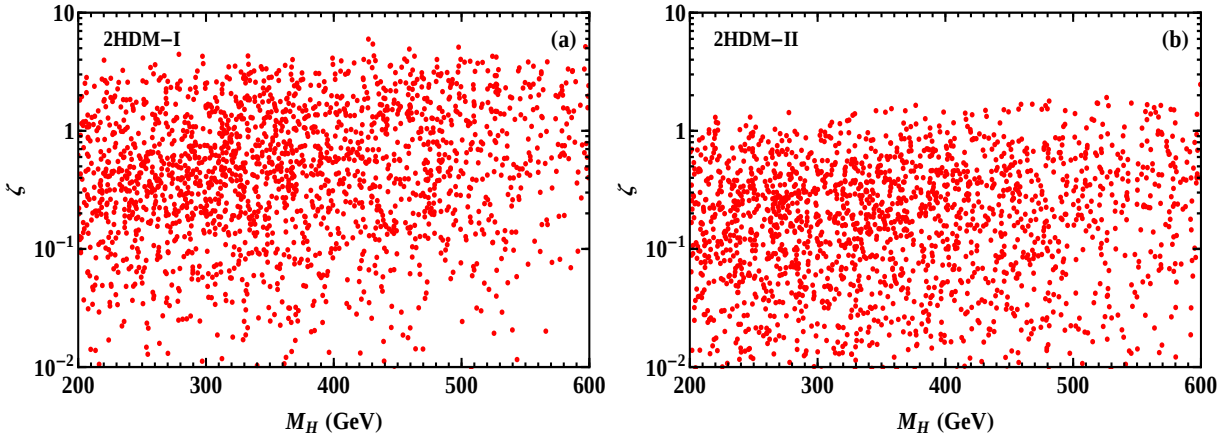

Figure 1: Parameter space in $M_H - \zeta$ plane for the 2HDM-I [plot-(a)] and 2HDM-II [plot-(b)], where the red dots present the viable points obeying the consistency requirement of the Higgs potential as explained in the text.

The Yukawa interactions of H with fermions can be expressed as follows

$$\mathcal{L}_{\mathrm{Y}(H)} \;=\; -\sum_{f=u,d,\ell} \frac{m_f}{v}\xi_H^f\, \bar{f} f\, H\,, \tag{5}$$

where the dimensionless coefficient ξ_H^f differs between the Type-I and Type-II of 2HDM, as summarized in Table 1.

Table 1: Summary of the Yukawa couplings ξ_H^f between the heavier Higgs boson H^0 and the SM fermions in 2HDM-I and 2HDM-II, where we have factorized out a common factor m_f/v (corresponding to the SM Higgs Yukawa coupling).

2HDM	ξ_H^u	ξ_H^d	ξ_H^ℓ
Type-I	$\sin\alpha/\sin\beta$	$\sin\alpha/\sin\beta$	$\sin\alpha/\sin\beta$
Type-II	$\sin\alpha/\sin\beta$	$\cos\alpha/\cos\beta$	$\cos\alpha/\cos\beta$

Inspecting the Higgs potential (1), we derive the scalar coupling of trilinear vertex Hhh,

$$\begin{aligned} G_{Hhh} &= \frac{\cos(\beta-\alpha)}{v}\left[\left(3M_A^2 - M_H^2 - 2M_h^2 + 3\lambda_5 v^2\right)\left(\cos 2(\beta-\alpha) - \frac{\sin 2(\beta-\alpha)}{\tan 2\beta}\right) - M_A^2 - \lambda_5 v^2\right] \\ &= \frac{\cos(\beta-\alpha)}{v}\left[\left(\frac{6M_{12}^2}{\sin 2\beta} - M_H^2 - 2M_h^2\right)\left(\cos 2(\beta-\alpha) - \frac{\sin 2(\beta-\alpha)}{\tan 2\beta}\right) - \frac{2M_{12}^2}{\sin 2\beta}\right], \end{aligned} \tag{6}$$

where in the second step we have used the relation $M_A^2 + \lambda_5 v^2 = 2M_{12}^2/\sin 2\beta$. In the SM, the cubic Higgs coupling $G_{hhh}^{\rm sm} = -3M_h^2/v$. We define a coupling ratio, $\zeta = G_{Hhh}/G_{hhh}^{\rm sm}$, which characterizes the relative strength of the Hhh coupling as compared to the h^3 Higgs coupling of the SM. Under alignment limit $\cos(\beta-\alpha) \to 0$, the trilinear scalar coupling (6) takes the asymptotical form,

$$\zeta \;=\; \frac{G_{Hhh}}{G_{hhh}^{\rm sm}} \;=\; \frac{(8M_{12}^2/\sin 2\beta - M_H^2 - 2M_h^2)}{3M_h^2}\cos(\beta-\alpha) + O(\cos^2(\beta-\alpha))\,. \tag{7}$$

In Fig. 1, we explore the parameter space of the Higgs potential (1) in the $M_H - \zeta$ plane. For $\zeta > 1$, we expect that the decay branching fraction $\mathrm{Br}[H \to hh]$ and the production cross section $\sigma[gg \to H \to hh]$ will be enhanced by the factor ζ^2. In Fig. 1, the red points present the viable parameter space consistent with vacuum stability, unitarity and perturbativity bounds of the Higgs potential [9]. We also take into account the 3σ constraints from the current Higgs global fit (cf. Sec. 4). For the analysis of Fig. 1, we have scanned the parameter space in the following range, $\tan\beta \in [1,\, 10]$, $\cos(\beta-\alpha) \in [-0.6,\, 0.6]$, $M_{12}^2 \in [-200^2,\, 200^2]\,\mathrm{GeV}^2$, $M_H \in [200,\, 600]\,\mathrm{GeV}$, and $M_A, M_{H^\pm} \in [300,\, 2000]\,\mathrm{GeV}$. In the following analysis, we will consider the same range of the 2HDM parameter space unless specified otherwise.

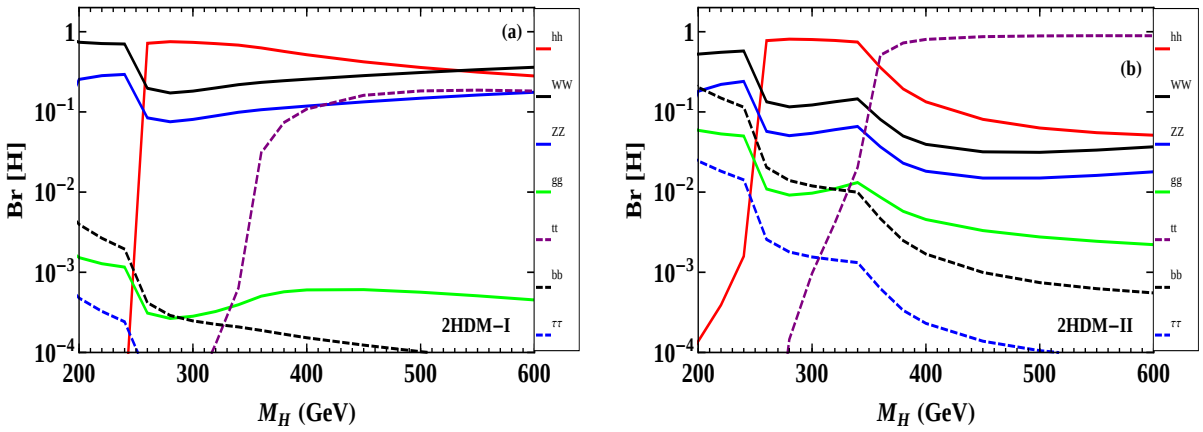

Figure 2: Decay branching fractions of the heavier Higgs state H^0 for the 2HDM-I [plot-(a)] and 2HDM-II [plot-(b)]. For illustration, we set $\tan\beta = 1$ and $(M_A,\, M_{12}^2) = (500\text{GeV},\, -(180\text{GeV})^2)$ for both plots. We also input $\cos(\beta-\alpha) = 0.4$ for plot-(a) and $\cos(\beta-\alpha) = 0.1$ for plot-(b).

2.2. Heavier Higgs Boson $\mathbf{H^0}$: Decays and Production

Let us consider the decay modes of the heavier neutral Higgs boson H^0. It is straightforward to infer the tree-level decay width for $M_H > 2M_h$,

$$\Gamma[H \to hh] \;=\; \frac{9\zeta^2 M_h^4}{32\pi v^2 M_H}\sqrt{1-\frac{4M_h^2}{M_H^2}}\;. \tag{8}$$

For $M_H \leqslant 2M_h$, we will include the off-shell decay $H \to hh^*$ with $h^* \to f\bar{f},\, gg,\, \gamma\gamma$, etc, where f denotes the light fermions except top quark. For the decay modes $H \to VV,\, f\bar{f}$, we have $\Gamma[H \to VV]/\Gamma[H \to VV]_{\rm sm} = \cos^2(\beta-\alpha)$ and $\Gamma[H \to f\bar{f}]/\Gamma[H \to f\bar{f}]_{\rm sm} = (\xi_H^f)^2$. For the decay channel $H \to gg$, we can express the partial width relative to the SM value, $\Gamma[H \to gg]/\Gamma[H \to gg]_{\rm sm} = |\sum_{f=t,b}\xi_H^f A_{1/2}^H(\tau_f)/A_{1/2}^H(\tau_t)|^2$, where $\tau_f = M_H^2/(4m_f^2)$ and the function $A_{1/2}^H(\tau_f)$ is the standard formula [9][16]. The decay branching ratio of $H \to \gamma\gamma$ is practically negligible for $M_H \gtrsim 200\,\text{GeV}$. In Fig. 2, we present the decay branching fractions of the heavier Higgs boson H for both 2HDM-I [plot-(a)] and 2HDM-II [plot-(b)]. For illustration, we input $\tan\beta = 1$ and $(M_A,\, M_{12}^2) = (500\text{GeV},\, -(180\text{GeV})^2)$ for both plots. We also set $\cos(\beta-\alpha) = 0.4$ for plot-(a) and $\cos(\beta-\alpha) = 0.1$ for plot-(b). We see that for $M_H < 250\,\text{GeV}$, the dominant decay channels are $H \to ZZ, WW$, and for $250\,\text{GeV} < M_H < 350\,\text{GeV}$, the major decay channels include $H \to ZZ, WW, hh$ since the $H \to hh$ channel opens up. For $M_H > 350\text{GeV}$, the $H \to t\bar{t}$ channel is further opened, and will become dominant in the 2HDM-II when $\cos(\beta-\alpha)$ takes values around the alignment limit as shown in Fig. 2(b). But this situation can change when $\cos(\beta-\alpha)$ becomes larger and falls into the allowed region which separates from the alignment region (cf. Fig. 9 in Sec. 4).

From Eq. (5) and Tabel 1, we see that the Yukawa coupling of the heavier Higgs boson H with $t\bar{t}$ has a scale factor $\xi_H^t = \sin\alpha/\sin\beta$ relative to the SM Higgs Yukawa coupling. The major LHC production channel is the gluon fusion process $gg \to H$. Other production processes include the vector boson fusion $pp \to Hjj$, the vector boson associated production $pp \to HV$, and the top associated production $gg \to Ht\bar{t}$. The gluon fusion production cross section of H can be obtained from the corresponding SM cross section with a rescaling by $H \to gg$ partial width,

$$\sigma[gg \to H] \;=\; (\Gamma[H \to gg]/\Gamma[H \to gg]_{\rm sm})\,\sigma[gg \to H]_{\rm sm}\,, \tag{9}$$

where we will include all NLO QCD corrections to the gluon fusion cross section as done in the SM case [17]. We note that for the 2HDM-I, Table 1 shows that the H Yukawa couplings with top and bottom quarks have the same structure as in the SM, so the H production cross section $\sigma[gg \to H]$ differs from the SM by a simple rescaling factor $(\sin\alpha/\sin\beta)^2$. For the 2HDM-II, we see that the H coupling to b quarks differs from that of t quarks by a factor of $\tan\beta/\tan\alpha$, which can enhance the b-loop contribution to the $gg \to H$ production for large $\tan\beta$ region. Hence, the general relation (9) should be used. The uncertainty of the gluon fusion cross section is about 10% over the mass-range $M_H = 250-600\,\text{GeV}$ [17], which is roughly the total uncertainty of signal and background calculations. For the inclusive H production, we include the gluon fusion $gg \to H$, and b-related processes $b\bar{b} \to H$, $gb/\bar{b} \to Hb/\bar{b}$, and $q\bar{q}/gg \to Hb\bar{b}$. We present the inclusive H production rate for the 2HDM in Fig. 3. Multiplying the production cross section with the decay branching fraction, we compute the signal rate in the channel[1] $pp \to H \to hh \to WW^*\gamma\gamma$.

[1] Our analysis of the production rate of $gg \to H \to hh$ in the 2HDM is consistent with the recent study [18]. We thank Yun Jiang and Jérémy Bernon for providing data points of their calculation for numerical comparison.

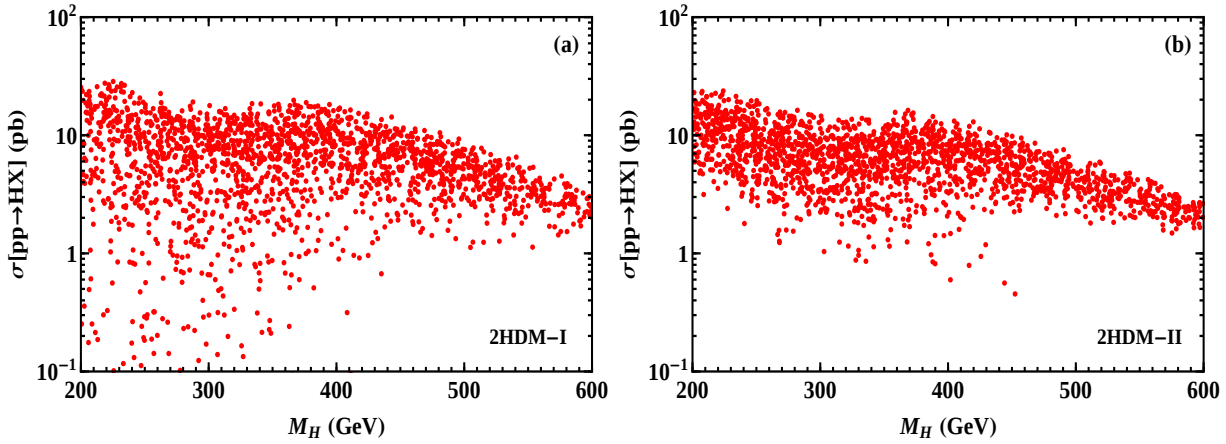

Figure 3: Inclusive H production cross section via $pp \to HX$ process at the LHC (14 TeV), for 2HDM-I [plot-(a)] and 2HDM-II [plot-(b)] with $\tan\beta \in [1, 10]$. All the red points satisfy the requirements of stability, perturbativity and unitarity, as well as the 3σ constraint by the current Higgs global fit.

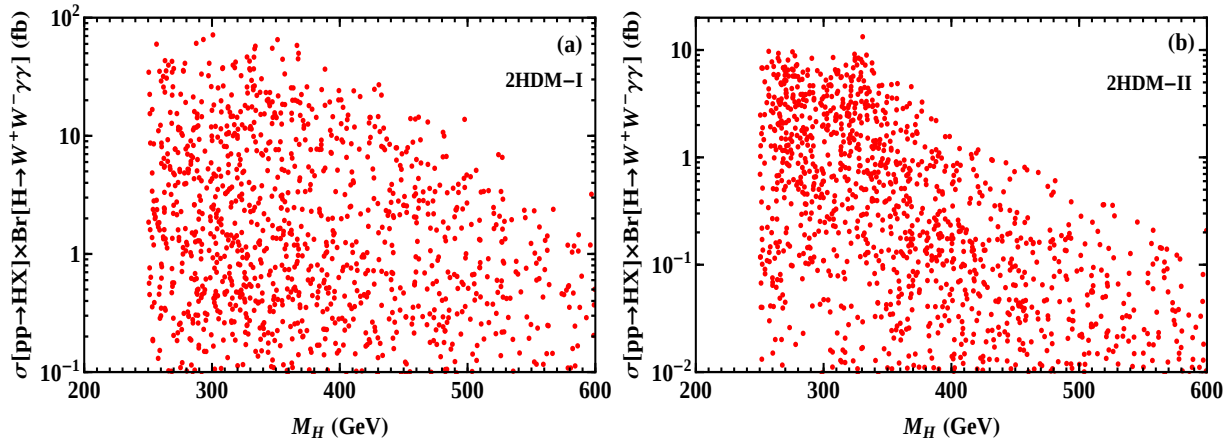

Figure 4: LHC signal cross section of $pp \to H \to hh \to WW^*\gamma\gamma$ in the 2HDM with $\tan\beta \in [1, 10]$. Plot-(a) presents the results for 2HDM-I and plot-(b) depicts 2HDM-II.

We summarize the results in Fig. 4 for Type-I and Type-II 2HDM, respectively. In Figs. 3–4, we have scanned the same 2HDM parameter space as in Fig. 1. The signal process is depicted by the left diagram of Fig. 5. From Fig. 4, we see that the cross section $pp \to H \to hh \to WW^*\gamma\gamma$ can be as large as about 70 fb for 2HDM-I; while for 2HDM-II, this cross section can reach about 10 fb for $M_H \lesssim 340$ GeV.

3. Higgs Signal and Background Simulations

In this section, we compute the Higgs signals and backgrounds at the LHC (14 TeV). We perform systematical simulations by using MadGraph5 package [19] for the process $pp \to H \to hh \to WW^*\gamma\gamma$. The corresponding Feynmann diagram is shown in the left diagram of Fig. 5. For signal process, we generate the model file using FeynRules [20], containing Hhh vertex and the effective ggH vertex. We compute signal and background events using MadGraph5/MadEvent [19]. Then, we apply Pythia [21] to simulate hadronization of partons and adopt Delphes [22] to perform detector simulations.

For the final state WW decays, we will study both the pure leptonic mode $WW \to \ell\nu\ell\nu$ and the semi-leptonic mode $WW \to q\bar{q}'\ell\nu$. The W decay branching fractions to $e\nu$ and $\mu\nu$ equal 10.8% and 10.6%, respectively, while that of $W \to \tau\nu$ is about 11.3% [23]. The dijet branching ratio of $W \to q\bar{q}'$ equals 67.6% [23]. Thus, the inclusion of semi-leptonic mode will be beneficial. Since τ leptons can decay into e, μ, the detected final state e, μ will include those from the τ decays. For $M_h = 125$ GeV, the branching fraction of $h \to \gamma\gamma$ in the SM equals 2.3×10^{-3} [16]. In the following, we will present the analyses for $M_H = 300$ GeV in Sec. 3.1–3.2, and for $M_H = 400, 600$ GeV in Sec. 3.3.

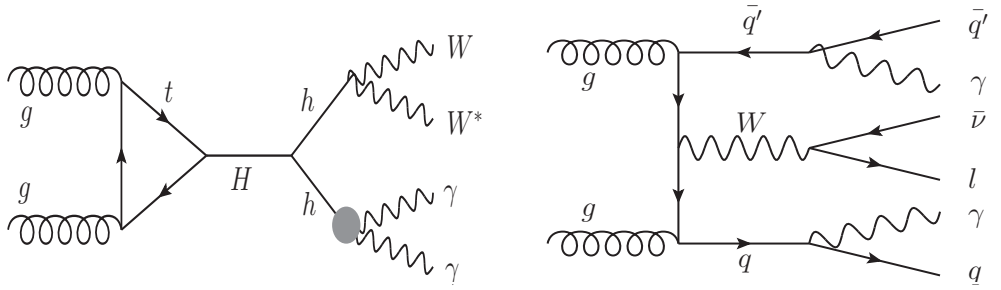

Figure 5: LHC production process $gg \to WW\gamma\gamma$. The left diagram shows the signal production $gg \to H \to hh \to WW\gamma\gamma$, and the right diagram illustrates an irreducible background process $gg \to q\bar{q}'\ell\bar{\nu}\gamma\gamma$.

3.1. **Pure Leptonic Channel:** $hh \to WW^*\gamma\gamma \to \ell\nu\ell\nu\gamma\gamma$

For pure leptonic channel, we have $hh \to WW^*\gamma\gamma \to \ell\nu\ell\nu\gamma\gamma$. Although this channel has an event rate about two orders of magnitude lower than that of $hh \to b\bar{b}\gamma\gamma$ mode, it has much cleaner background as compared to $b\bar{b}\gamma\gamma$ final state. After imposing simple cuts, we find that the backgrounds can be substantially reduced. We follow the ATLAS procedure for event selections. To discriminate the Higgs signal from backgrounds, we set up preliminary event selection by requiring two leptons (electron or muon) and at least two photons in the final state,

$$n_\ell = 2\,, \qquad n_\gamma \geqslant 2\,. \tag{10}$$

In the first step of event analysis, we need to prevent the potential double-counting, i.e., the reconstructed objects are required to have a minimal spatial separation [24]. The two leading photons are always kept, but we impose the following criteria [24]: (i) electrons overlapping with one of those photons within a cone $\Delta R(e,\gamma) < 0.4$ are rejected; (ii) jets within $\Delta R(\text{jet}, e) < 0.2$ or $\Delta R(\text{jet},\gamma) < 0.4$ are rejected; (iii) muons within a cone of $\Delta R(\mu, \text{jet}) < 0.4$ or $\Delta R(\mu,\gamma) < 0.4$ are rejected. After this, we apply the basic cuts to take into account the detector conditions, which are imposed as follows,

$$P_T(\gamma), P_T(q) > 25\,\text{GeV}, \quad P_T(\ell) > 15\,\text{GeV}, \quad |\eta(\gamma)|, |\eta(q)|, |\eta(\ell)| < 2.5\,. \tag{11}$$

Then, we impose cuts on the diphoton invariant-mass $M_{\gamma\gamma}$ and the missing energy $\not{E}_T$ of final state neutrinos,

$$120\,\text{GeV} < M_{\gamma\gamma} < 130\,\text{GeV}, \qquad \not{E}_T > 20\,\text{GeV}\,. \tag{12}$$

The missing energy cut can also sufficiently remove the $\ell\ell\gamma\gamma$ background.

For the transverse mass cut [23], we consider the transverse mass M_T for the $\ell\ell\nu\nu$ system with two leptons and missing energy, which should be no larger than the Higgs mass M_h. All the final state leptons/neutrinos are nearly massless, so the transverse energy of each final state equals its transverse momentum $E_{T,i} \simeq |\vec{P}_{T,i}|$, $(i = 1,2,3)$, where $i = 1,2$ denote two leptons $\ell_{1,2}$ and $i = 3$ denotes the system of two neutrinos. Thus, we have

$$M_T^2 \;=\; (E_{T,1} + E_{T,2} + E_{T,3})^2 - (\vec{P}_{T,1} + \vec{P}_{T,2} + \vec{P}_{T,3})^2 \;=\; \sum_{1\leqslant i<j\leqslant 3} 2E_{T,i}E_{T,j}(1-\cos\phi_{ij})\,. \tag{13}$$

With this, we impose the transverse mass cut

$$60\text{GeV} \;<\; M_T(\ell\ell\nu\nu\gamma\gamma) \;<\; 300\,\text{GeV}\,. \tag{14}$$

Finally, we apply the kinematical cuts on the azimuthal angle $\Delta\phi$ and opening angle ΔR of the two final state leptons,

$$\Delta\phi(\ell\ell) < 1.5\,, \qquad \Delta R(\ell\ell) < 1.8\,. \tag{15}$$

We present the distributions of these kinematical variables in Fig. 6. In this figure, we show the signal distributions at the LHC (14TeV) with 300 fb^{-1} integrated luminosity for $M_H = (300,\ 400,\ 600)$ GeV by (red, green, blue) curves as well as the backgrounds (black curves). Here we have input the sample cross section $\sigma(pp \to H \to hh \to WW^*\gamma\gamma) = (5,\ 3,\ 1)$ fb for $M_H = (300,\ 400,\ 600)$ GeV, respectively. The kinematical cuts for the cases of $M_H = 400,\ 600$ GeV will be discussed in Sec. 3.3.

Next, we turn to the background analysis for pure leptonic mode. Besides the $\ell\nu\ell\nu\gamma\gamma$ and $\ell\ell\gamma\gamma$ backgrounds, there are additional reducible backgrounds from Higgs bremstrahlung, vector boson fusion, and $t\bar{t}h$ production. The cross section of the former two processes are fairly small and thus negligible for the present study. The $t\bar{t}h$ associate production, with $t\bar{t} \to WWb\bar{b}$, can be important because the diphoton invariant-mass cut does not effectively discriminate the signal process. But, this background can be suppressed by imposing b-veto [25]. The production cross

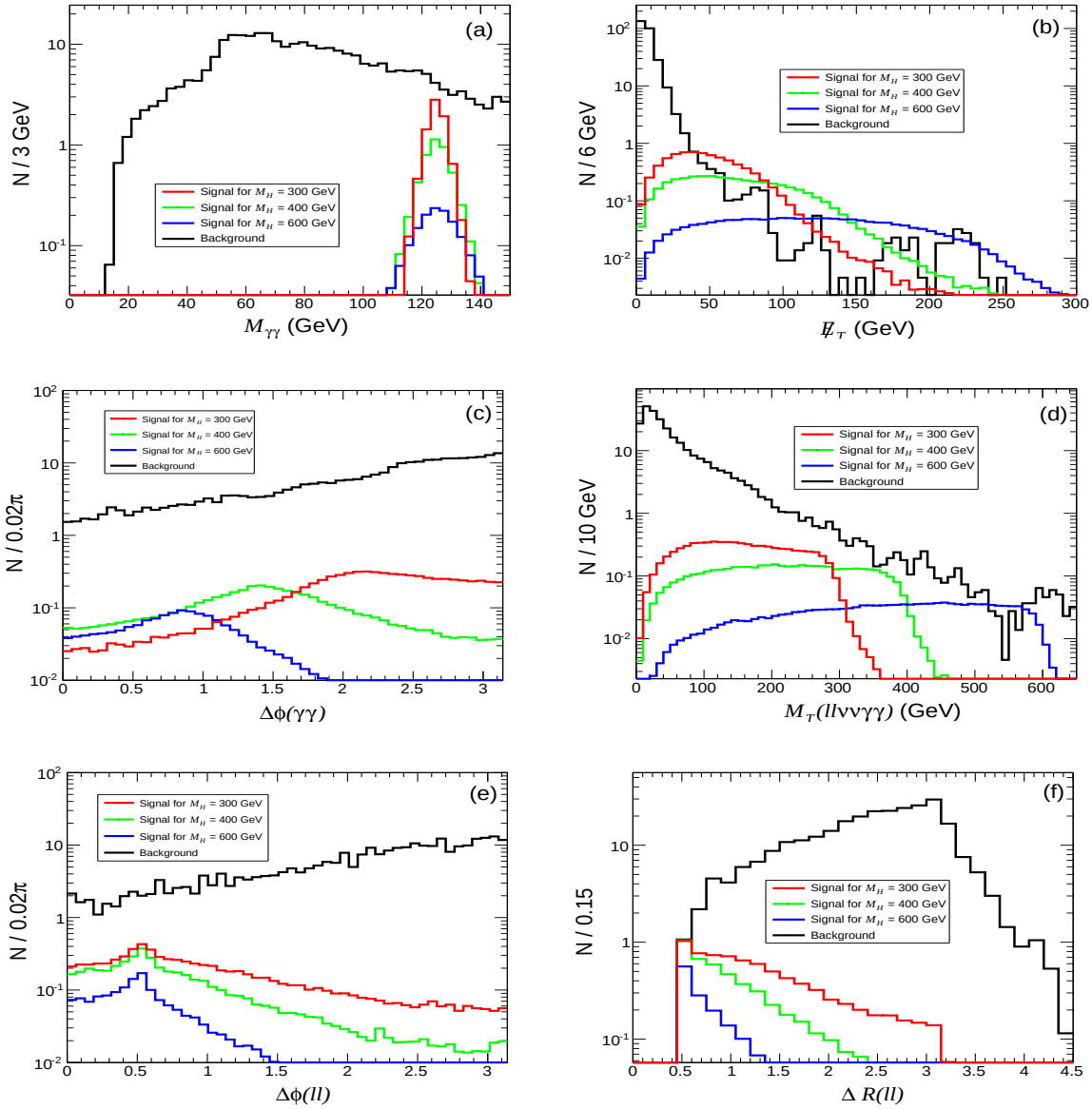

Figure 6: Signal and background distributions in the pure leptonic channel $hh \to WW^* \to \ell\nu\ell\nu$ before imposing kinematical cuts, at the LHC (14TeV) with 300 fb^{-1} integrated luminosity. For comparison, we present the signal distributions for M_H = 300, 400, 600 GeV in red, green, and blue curves, respectively. Plot-(a) shows the $M_{\gamma\gamma}$ distribution; plot-(b) depicts the $\not{E}_T$ distribution; plot-(c) shows the $\Delta\phi_{\gamma\gamma}$ distribution; plot-(d) gives the $M_T(\ell\ell\nu\nu\gamma\gamma)$ distribution; plot-(e) displays the $\Delta\phi_{\ell\ell}$ distribution; and plot-(f) presents the $\Delta R_{\ell\ell}$ distribution.

section for $t\bar{t}h$ in the SM is $\sigma(pp \to t\bar{t}h) = 0.6113$ pb [26]. Taking the b-veto efficiency $\epsilon(b\text{−veto}) = 30\%$, we estimate the cross section for this background process,

$$\sigma(pp \to t\bar{t}h \to \ell\nu\ell\nu\gamma\gamma) \;=\; \sigma(pp \to t\bar{t}h) \times \mathrm{Br}[W \to \ell\nu]^2\, \mathrm{Br}[h \to \gamma\gamma]\, \epsilon(b\text{−veto})^2 \simeq 1.3\times10^{-2}\ \mathrm{fb}\,, \tag{16}$$

where $W \to \ell\nu$ includes $\ell = e, \mu, \tau$. We see that imposing the b-veto makes the $t\bar{t}h$ background much less relevant.

Other reducible backgrounds come from the fake events in which quark and/or gluon are misidentified as photons. These backgrounds include $\ell\nu\ell\nu qq\gamma$, $\ell\nu\ell\nu g\gamma$, $\ell\nu\ell\nu qq$, $\ell\nu\ell\nu qg$, and $\ell\nu\ell\nu gg$. For our analysis, we adopt the fake rates used by ATLAS detector [28],

$$\epsilon_{q\to\gamma} \simeq 3.6\times10^{-4}, \qquad \epsilon_{g\to\gamma} \simeq 3.6\times10^{-5}. \tag{17}$$

With such small fake rates, we find that these reducible backgrounds are negligible. Hence, under the above considerations, we only need to count on the irreducible SM backgrounds with final state $\ell\nu\ell\nu\gamma\gamma$.

We summarize the results in Table 2 for both signal and backgrounds. For illustration, we input the heavier Higgs mass M_H = 300 GeV, and set the sample signal cross section $\sigma(pp \to H \to hh \to WW^*\gamma\gamma)$ = 5 fb for the LHC (14 TeV). In Table 2, we also show the significance of signal over backgrounds after each kinematical cut at the LHC Run-2 with 300 fb^{-1} integrated luminosity. When the event number is small, we can use the median significance(Z_0) (instead of $S/\sqrt{B}$), defined as follows [27],

$$Z_0 = \sqrt{2\left[(S+B)\ln\left(\frac{S+B}{B}\right) - S\right]}\,. \tag{18}$$

Table 2: Signal and background cross sections of $pp \to WW^*\gamma\gamma \to \ell\nu\ell\nu\gamma\gamma$ and $pp \to WW^*\gamma\gamma \to q\bar{q}'\ell\nu\gamma\gamma$ processes at the LHC (14 TeV) after each cut. The signal strengths, $S/\sqrt{B}$ and significance(Z_0), are computed for the LHC (14 TeV) with 300 fb^{-1} integrated luminosity. We input the heavier Higgs mass $M_H = 300$ GeV, and the sample signal cross section is set as $\sigma(pp \to H \to hh \to WW^*\gamma\gamma) = 5$ fb.

$pp \to \ell\nu\ell\nu\gamma\gamma$	Sum	Selection+Basic Cuts	$M_{\gamma\gamma}$, $\not{E}_T$	$M_T(\ell\ell\nu\nu\gamma\gamma)$, $\Delta\phi(\ell\ell)$, $\Delta R(\ell\ell)$
Signal (fb)	0.525	0.0257	0.019	0.0141
B[$\ell\nu\ell\nu\gamma\gamma + \ell\ell\gamma\gamma$] (fb)	153	0.935	0.00127	0.000153
$S/\sqrt{B}$	0.735	0.46	9.23	19.8
Significance(Z_0)	0.735	0.458	4.72	5.51
$pp \to q\bar{q}'\ell\nu\gamma\gamma$	Sum	Selection+Basic Cuts	$M_{\gamma\gamma}$, M_{qq}, $\not{E}_T$	$P_T(\gamma)$, $M_T(q\bar{q}'\ell\nu)$
Signal (fb)	2.2	0.125	0.035	0.028
B[$q\bar{q}'\ell\nu\gamma\gamma$] (fb)	31.59	0.58	0.0015	0.00063
B[$\ell\nu\gamma\gamma$] (fb)	143.3	0.064	0.00072	0.00033
B[Wh] (fb)	0.42	0.0051	0.00025	0.00014
B[WWh] (fb)	0.0023	0.00021	0.00002	0.00001
S/B	0.0125	0.193	14.1	25.2
$S/\sqrt{B}$	2.88	2.69	12.1	14.6
Significance(Z_0)	2.87	2.61	6.33	6.34

As shown in Table 2, after applying all kinematical cuts (except the $\Delta R(\ell\ell)$ cut), we deduce the signal significance $Z_0 = 5.51$.

3.2. **Semi-leptonic Channel:** $hh \to WW^*\gamma\gamma \to q\bar{q}'\ell\nu\,\gamma\gamma$

The analysis of semi-leptonic channel $WW^* \to q\bar{q}'\ell\nu$ is similar to that of the pure leptonic mode $WW^* \to \ell\nu\ell\nu$. But, there are also some differences. One thing is that for each decay we need to specify which decay mode is from on-shell W ($q\bar{q}'$ or $\ell\nu$), since these two situations have different distributions. To illustrate this, we present the distribution of M_{qq} in Fig. 7, where the green (blue) curve depicts the final state qq from on-shell (off-shell) W decays, and the red curve represents the actual distribution of M_{qq} from $WW^* \to q\bar{q}'\ell\nu$. Fig. 7 shows that the M_{qq} distribution from on-shell W decays (green curve) has event rate peaked around $M_{qq} = 70 - 80$ GeV, while the M_{qq} distribution from off-shell W decays (blue curve) is rather flat.

Our first step here is also to remove the pileup events, similar to Sec. 3.1. Then, we select the final states by imposing the preliminary cuts

$$n_j \geqslant 2\,, \quad n_\gamma \geqslant 2\,, \quad n_\ell = 1\,. \tag{19}$$

For jets we choose the leading and subleading pair, while for photons we choose the diphoton pair whose $M_{\gamma\gamma}$ is closet to $M_h = 125$ GeV. Then, we choose the basic cuts to be the same as in Eq. (11), and the $M_{\gamma\gamma}$ cut as in Eq. (12). The invariant-mass M_{qq} should match the W mass. We depict the M_{qq} distribution in Fig. 7. Plot-(a) depicts the decay mode with on-shell (off-shell) decays $W\,(W^*) \to q\bar{q}'$ by green (blue) curve, for $M_H = 300$ GeV. The realistic decays of $WW^* \to q\bar{q}'\ell\nu$ correspond to the red curve. In plot-(b), we present the M_{qq} distribution for full signals of $WW^* \to q\bar{q}'\ell\nu$ by (red, green, blue) curves for $M_H = (300,\ 400,\ 600)$ GeV. The black solid curve in each plot gives the full backgrounds. From Fig. 7, we choose the M_{qq} cut

$$M_{qq} < 90\,\text{GeV}. \tag{20}$$

We present the distributions for other kinematical observables in Fig. 8, where we have input the sample cross section $\sigma(pp \to H \to hh \to WW^*\gamma\gamma) = (5,\ 3,\ 1)$ fb for $M_H = (300,\ 400,\ 600)$ GeV. From Fig. 8(a)-(b), we impose cuts on the diphoton invariant-mass $M_{\gamma\gamma}$ and the missing energy $\not{E}_T$ of final state neutrinos,

$$120\,\text{GeV} < M_{\gamma\gamma} < 130\,\text{GeV}, \qquad 10\,\text{GeV} < \not{E}_T < 40\,\text{GeV}. \tag{21}$$

We require $\not{E}_T > 10$ GeV to suppress certain reducible backgrounds, as also adopted in ATLAS analysis. For instance, consider the background $qqj\gamma\gamma$ with j mistagged as a lepton. Since it contains no neutrino in the final state, we can remove it by imposing the missing energy $\not{E}_T$ cut. This is more like a basic cut. For the transverse momentum distribution of the leading photon shown in Fig. 8(d), we set the following cut

$$60\,\text{GeV} < P_T(\gamma) < 120\,\text{GeV}. \tag{22}$$

Then, we inspect the transverse mass distribution of $q\bar{q}'\ell\nu$ final state, which arises from the decay products of $h \to WW^* \to q\bar{q}'\ell\nu$. From Fig. 8(c), we impose the following cut

$$M_T(q\bar{q}'\ell\nu) < 150\,\text{GeV}. \tag{23}$$

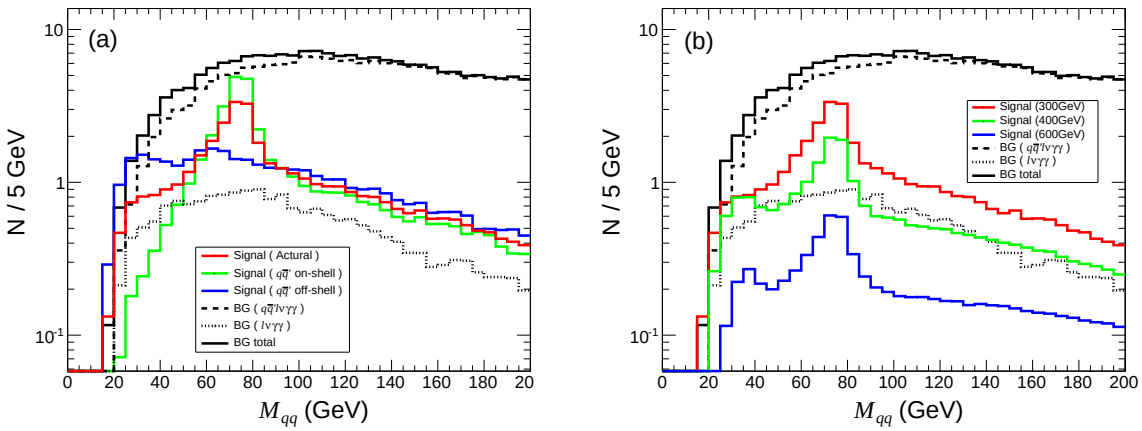

Figure 7: Invariant-mass distribution of M_{qq} for the decay channel $WW^* \to q\bar{q}'\ell\nu$ at the LHC (14TeV) with 300 fb^{-1} integrated luminosity. Plot-(a) shows the mode with on-shell (off-shell) decays $W\,(W^*) \to q\bar{q}'$ by green (blue) curve, for $M_H = 300$ GeV. The red curve corresponds to the realistic decays of $WW^* \to q\bar{q}'\ell\nu$. Plot-(b) presents the M_{qq} distribution for full signals of $WW^* \to q\bar{q}'\ell\nu$ by (red, green, blue) curves for $M_H = (300,\ 400,\ 600)$ GeV. In each plot, the black solid curve gives the full backgrounds.

With Fig. 8(e)-(f), we have also examined possible cuts on $\Delta\phi(\gamma\gamma)$ and $\Delta R(\gamma\gamma)$ distributions. But we find no significant improvement of sensitivity for the case of $M_H = 300$ GeV.

Next, we turn to the background analysis, as shown by the black curves in Fig. 8. The most important background for this channel comes from the SM irreducible background, $pp \to q\bar{q}'\ell\nu\gamma\gamma$, whose cross section is about $\sigma[q\bar{q}'\ell\nu\gamma\gamma] \simeq 31.6$ fb. Another significant reducible background is the SM process $pp \to \ell\nu\gamma\gamma$, which has a cross section $\sigma[\ell\nu\gamma\gamma] \simeq 143$ fb. But this will be mainly rejected by the jet-selections (19), as shown in Table 2. Other potential SM backgrounds may include the reducible backgrounds such as $qq\ell\nu gg$ with gg misidentified as $\gamma\gamma$. This is actually negligible due to the tiny $g \to \gamma$ misidentification rate given in Eq. (17).

We summarize our results in Table 2. Here we present the signal and background cross sections after each cuts. We take an integrated luminosity of 300 fb^{-1} for the LHC (14 TeV), and derive the corresponding signal strength $S/\sqrt{B}$ and significance(Z_0). Under all cuts, we estimate the final significance of the signal detection to be 6.34 in the semi-leptonic channel $q\bar{q}'\ell\nu\gamma\gamma$, as shown in Table 2.

3.3. Analyses of Heavier Higgs Boson with 400 GeV and 600 GeV Masses

For signal and background analyses in Sec. 3.1–3.2, we have set the mass of heavier Higgs boson $M_H = 300$ GeV for demonstration. In this subsection, we turn to the analyses for other sample inputs of Higgs mass, $M_H = 400$ GeV and $M_H = 600$ GeV. We illustrate how the analysis and results may vary as the Higgs mass increases. These are parallel to what we have done in Sec. 3.1–3.2.

For the heavier Higgs boson with mass $M_H = 400$ GeV, from the distributions in Fig. 6, we choose the following kinematical cuts for the final state $\ell\nu\ell\nu\gamma\gamma$,

$$120\,\text{GeV} < M_{\gamma\gamma} < 130\,\text{GeV}, \quad \not{E}_T > 20\,\text{GeV}, \quad 75\text{GeV} < M_T(\ell\nu\ell\nu\gamma\gamma) < 400\,\text{GeV}, \tag{24a}$$

$$\Delta\phi(\ell\ell) < 1.5\,, \quad \Delta R(\ell\ell) < 1.5\,, \quad \Delta\phi(\gamma\gamma) < 2.0\,, \quad \Delta R(\gamma\gamma) < 2.3\,. \tag{24b}$$

Comparing with the previous case of $M_H = 300$ GeV, we see from Fig. 6 that we can add tighter cuts (24b) on $\Delta\phi(\ell\ell)$ and $\Delta R(\ell\ell)$ for di-leptons, and on $\Delta\phi(\gamma\gamma)$ and $\Delta R(\gamma\gamma)$ for di-photons, since the lighter Higgs bosons hh are more boosted in the final state for $M_H = 400$ GeV. Fig. 6 also shows that the signal distribution of $M_{\gamma\gamma}$ becomes lower and fatter. We present the cut efficiency for the case of $M_H = 400$ GeV in Table 3, where we set a sample signal cross section $\sigma(pp \to H \to hh \to WW^*\gamma\gamma) = 3$ fb. In this case, we derive a significance $Z_0 = 4.47$ after all the kinematical cuts. We also note from Fig. 4(a)-(b) that in 2HDM-I the cross section of $pp \to H \to hh \to WW^*\gamma\gamma$ can reach up to 30 fb for $M_H = 400$ GeV, while in 2HDM-II this cross section is below about 2 fb at $M_H = 400$ GeV. So the significance for probing the 2HDM-II with $M_H = 400$ GeV will be rescaled accordingly.

We further analyze semi-leptonic channels for detecting the heavier Higgs boson H with mass $M_H = 400$ GeV. The corresponding signal and background distributions are shown in Fig. 8. Inspecting these distributions, we choose the following kinematical cuts,

$$\begin{aligned} &120\,\text{GeV} < M_{\gamma\gamma} < 130\,\text{GeV}, \quad M_{qq} < 90\,\text{GeV}, \\ &80\,\text{GeV} < P_T(\gamma) < 180\,\text{GeV}, \quad M_T(q\bar{q}'\ell\nu) < 150\,\text{GeV}, \quad \not{E}_T > 10\,\text{GeV}, \\ &\Delta\phi(\gamma\gamma) < 1.9\,, \qquad 1.0 < \Delta R(\gamma\gamma) < 2.1\,. \end{aligned} \tag{25}$$

We summarize the cut efficiency of $qq\ell\nu\gamma\gamma$ final state for $M_H = 400$ GeV in Table 3. We derive a significance $Z_0 = 4.95$ after all the cuts.

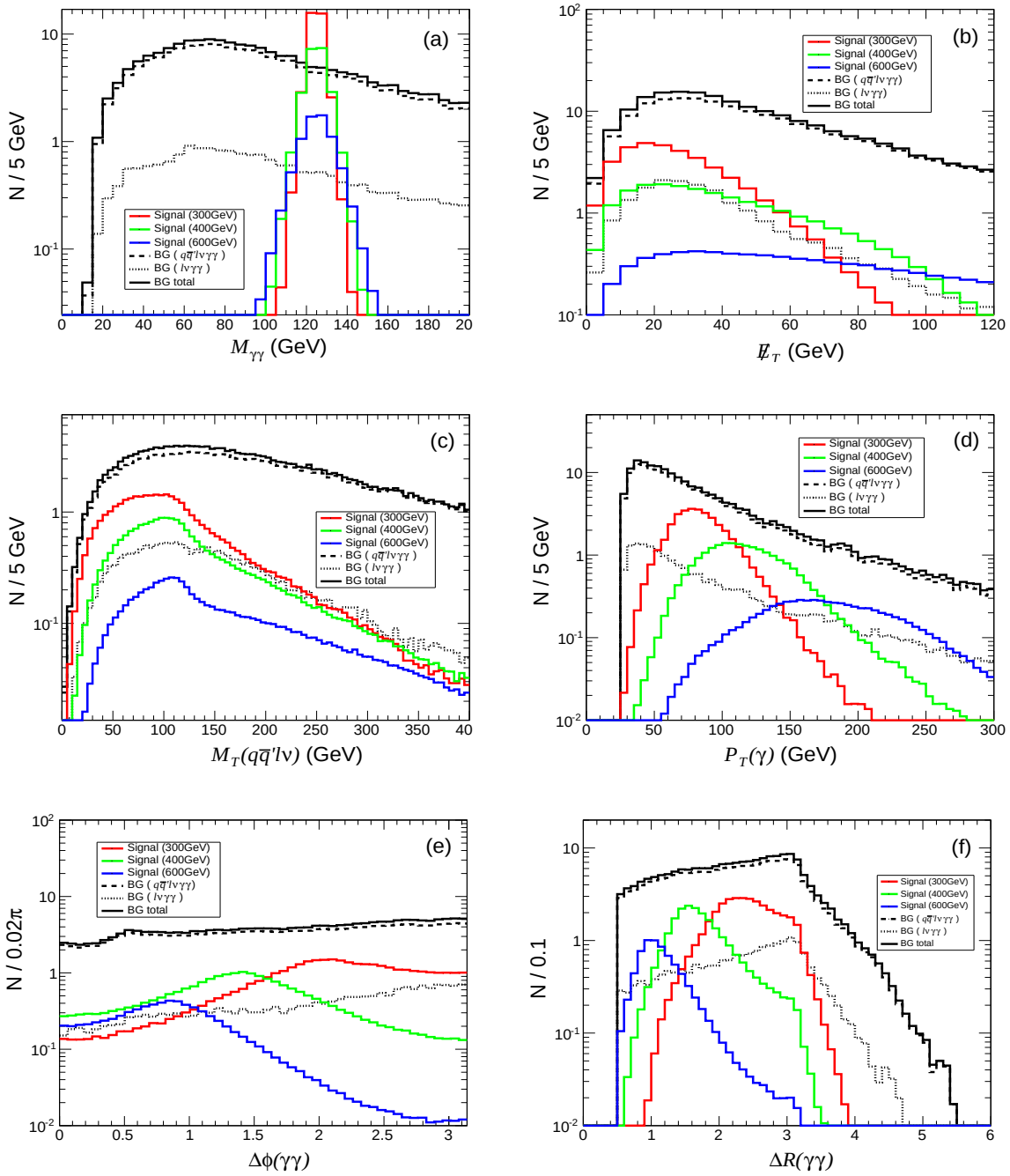

Figure 8: Signal and background distributions for semi-leptonic channel $hh \to WW^* \to q\bar{q}'\ell\nu\gamma\gamma$ before imposing kinematical cuts, at the LHC (14TeV) with 300 fb^{-1} integrated luminosity. For comparison, we present the signal distributions for $M_H = 300,\ 400,\ 600\,\text{GeV}$ in red, green, and blue curves, respectively. Plot-(a) shows the distribution of $M_{\gamma\gamma}$; plot-(b) depicts the missing energy $\not{E}_T$ distribution; plot-(c) presents the P_T distribution of the leading photon; and plot-(d) gives the transverse mass distribution of $M_T(q\bar{q}'\ell\nu)$.

For the heavier Higgs H with mass $M_H = 600\,\text{GeV}$, the distributions of pure leptonic mode are shown in Fig. 6. From these, we choose the following kinematical cuts

$$115\,\text{GeV} < M_{\gamma\gamma} < 135\,\text{GeV}, \quad \not{E}_T > 30\,\text{GeV}, \quad 75\,\text{GeV} < M_T(\ell\nu\ell\nu\gamma\gamma) < 600\,\text{GeV}, \tag{26a}$$

$$\Delta\phi(\ell\ell) < 1.2\,, \quad \Delta R(\ell\ell) < 1.5\,, \quad \Delta\phi(\gamma\gamma) < 1.6\,, \quad \Delta R(\gamma\gamma) < 1.8\,. \tag{26b}$$

The cut efficiency for $M_H = 600\,\text{GeV}$ is summarized in Table 4.

For the semi-leptonic final state $q\bar{q}'\ell\nu\gamma\gamma$ with $M_H = 600\,\text{GeV}$, we choose the kinematical cuts

$$\begin{aligned} &115\,\text{GeV} < M_{\gamma\gamma} < 135\,\text{GeV}, \quad M_{qq} < 90\,\text{GeV}, \\ &P_T(\gamma) > 120\,\text{GeV}, \quad M_T(q\bar{q}'\ell\nu) < 150\,\text{GeV}, \quad \not{E}_T > 10\,\text{GeV}, \\ &\Delta\phi(\gamma\gamma) < 1.4\,, \quad \Delta R(\gamma\gamma) < 1.7\,. \end{aligned} \tag{27}$$

With these, we summarize the cut efficiency of $q\bar{q}'\ell\nu\gamma\gamma$ final state for $M_H = 600\,\text{GeV}$ in Table 4. Since the typical production cross section with $M_H = 600\,\text{GeV}$ becomes significantly smaller over the parameter space, we take a sam-

Table 3: Signal and background cross sections of $pp \to WW^*\gamma\gamma \to \ell\nu\ell\nu\gamma\gamma$ and $pp \to WW^*\gamma\gamma \to q\bar{q}'\ell\nu\gamma\gamma$ processes at the LHC (14 TeV) after each cut. The signal strengths, $S/\sqrt{B}$ and significance(Z_0), are computed for the LHC (14 TeV) with 300 fb^{-1} integrated luminosity. We input the heavier Higgs mass $M_H = 400$ GeV, and set the sample signal cross section $\sigma(pp \to H \to hh \to WW^*\gamma\gamma) = 3$ fb.

$pp \to \ell\nu\ell\nu\gamma\gamma$	Sum	Selection+Basic Cuts	$M_{\gamma\gamma}$, $\not{E}_T$	$M_T(\ell\ell\nu\nu\gamma\gamma)$, $\Delta\phi(\ell\ell)$, $\Delta R(\ell\ell)$
Signal (fb)	0.315	0.0162	0.0137	0.0102
$B[\ell\nu\ell\nu\gamma\gamma + \ell\ell\gamma\gamma]$ (fb)	153	0.935	0.00251	0.000153
$S/\sqrt{B}$	0.44	0.291	4.73	14.2
Significance(Z_0)	0.44	0.29	3.14	4.47
$pp \to q\bar{q}'\ell\nu\gamma\gamma$	σ_{total}	Selection+Basic Cuts	$M_{\gamma\gamma}$, M_{qq}, $P_T(\gamma)$	$M_T(qq\ell\nu)$, $\Delta R_{\gamma\gamma}$, $\Delta\Phi_{\gamma\gamma}$
Signal (fb)	1.32	0.09	0.0216	0.0153
B$[qq\ell\nu\gamma\gamma]$ (fb)	31.6	0.58	0.0015	0.0003
B$[\ell\nu\gamma\gamma]$ (fb)	143	0.064	0.00053	0.00004
B$[Wh]$ (fb)	0.42	0.0051	0.0004	0.0001
B$[WWh]$ (fb)	0.0023	0.00021	0.000027	0.000006
S/B	0.00753	0.139	8.79	34.3
$S/\sqrt{B}$	1.73	1.93	7.55	12.5
Significance(Z_0)	1.72	1.89	4.47	4.95

Table 4: Signal and background cross sections of $pp \to WW^*\gamma\gamma \to \ell\nu\ell\nu\gamma\gamma$ and $pp \to WW^*\gamma\gamma \to q\bar{q}'\ell\nu\gamma\gamma$ processes at the LHC (14 TeV) after each cut. The signal strengths, $S/\sqrt{B}$ and significance(Z_0), are computed for the LHC (14 TeV) with 3 ab^{-1} integrated luminosity. We input the heavier Higgs mass $M_H = 600$ GeV, and set the sample signal cross section $\sigma(pp \to H \to hh \to WW^*\gamma\gamma) = 1$ fb.

$pp \to \ell\nu\ell\nu\gamma\gamma$	Sum	Selection+Basic Cuts	$M_{\gamma\gamma}$, $\not{E}_T$	$M_T(\ell\ell\nu\nu\gamma\gamma)$, $\Delta\phi(\ell\ell)$, $\Delta R(\ell\ell)$
Signal (fb)	0.105	0.0057	0.0026	0.0023
$B[\ell\nu\ell\nu\gamma\gamma + \ell\ell\gamma\gamma]$ (fb)	153	0.94	0.000031	0.000015
$S/\sqrt{B}$	0.464	0.322	25.6	32.5
Significance(Z_0)	0.464	0.322	7.38	7.50
$pp \to q\bar{q}'\ell\nu\gamma\gamma$	σ_{total}	Selection+Basic Cuts	$M_{\gamma\gamma}$, M_{qq}, $P_T(\gamma)$	$M_T(qq\ell\nu)$, $\Delta R_{\gamma\gamma}$, $\Delta\Phi_{\gamma\gamma}$
Signal (fb)	0.44	0.03	0.0072	0.0051
B$[qq\ell\nu\gamma\gamma]$ (fb)	31.6	0.58	0.0015	0.0003
B$[\ell\nu\gamma\gamma]$ (fb)	143.	0.064	0.00053	0.00004
B$[Wh]$ (fb)	0.42	0.0051	0.0004	0.0001
B$[WWh]$ (fb)	0.0023	0.00021	0.000027	6×10^{-6}
S/B	0.00251	0.0462	2.93	11.4
$S/\sqrt{B}$	1.82	2.04	7.96	13.2
Significance(Z_0)	1.82	2.02	6.01	7.30

ple input $\sigma(pp \to H \to hh \to WW^*\gamma\gamma) = 1$ fb, and consider an integrated luminosity of 1 ab^{-1} at the LHC (14 TeV). Thus, from Table 4, we can estimate the significance $Z_0 = 4.33$ and 4.21 for the channels $WW^*\gamma\gamma \to \ell\nu\ell\nu\gamma\gamma$ and $WW^*\gamma\gamma \to q\bar{q}'\ell\nu\gamma\gamma$, respectively. Besides, from Fig. 4(a)-(b) we see that for $M_H = 600$ GeV, the cross section of $pp \to H \to hh \to WW^*\gamma\gamma$ in 2HDM-I can reach up to 3 fb, while this cross section in 2HDM-II is below about 0.2 fb. So the significance for probing the 2HDM-II with $M_H = 600$ GeV will be rescaled accordingly. In the following Sec. 4, we will give a general analysis of the significance by scanning the parameter space of 2HDM-I and 2HDM-II (Fig. 9) without assuming a sample cross section.

Finally, we note that the above analyses of Table 2–4 have taken the sample cross sections, $\sigma(pp \to H \to hh \to WW^*\gamma\gamma) = (5,\ 3,\ 1)$ fb and an integrated luminosity of $(300, 300, 3000)$ fb^{-1} for $M_H = (300,\ 400,\ 600)$ GeV. We have derived the significance of detecting H in each case. Thus, we may estimate the combined significance(Z_0) by including both the pure leptonic and semi-leptonic channels,

$$Z_0(\text{combined}) = \sqrt{Z_0^2(\ell\nu\ell\nu\gamma\gamma) + Z_0^2(q\bar{q}'\ell\nu\gamma\gamma)} \simeq (8.40,\ 6.67,\ 10.5)\,, \tag{28}$$

for $M_H = (300,\ 400,\ 600)$ GeV, and the corresponding integrated luminosity of $(300, 300, 3000)$ fb^{-1}.

4. Probing the 2HDM Parameter Space

In this section, we study the probe of the 2HDM parameter space by using the LHC detection of the heavier Higgs state H^0 via $pp \to H \to hh \to WW^*\gamma\gamma$ (Sec. 3), as well as the current global fit for the lighter Higgs boson

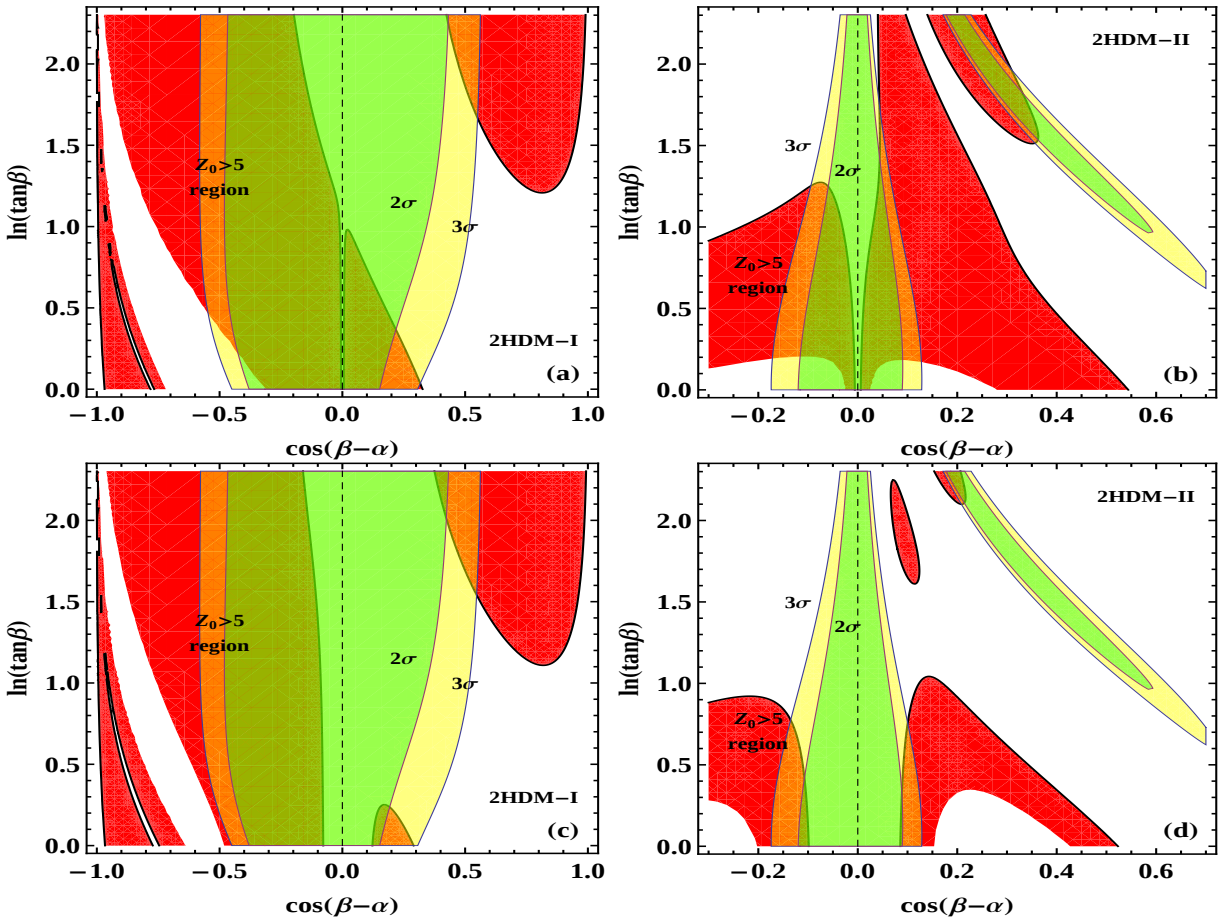

Figure 9: LHC probe of the 2HDM parameter space in $\cos(\beta-\alpha)-\tan\beta$ plane. We impose projected sensitivity of the LHC Run-2 by requiring significance$(Z_0) \geqslant 5$ for the process $pp \to H \to hh \to WW^*\gamma\gamma$, with 300 fb^{-1} integrated luminosity at $\sqrt{s} = 14$ TeV. The red contours correspond to significance$(Z_0) = 5$. Plots (a)-(b) [plots (c)-(d)] present the results for $M_H = 300$ GeV [$M_H = 400$ GeV], while plots (a) and (c) [plots (b) and (d)] give the results for 2HDM-I [2HDM-II]. The green (yellow) contours present the 2σ (3σ) constraints from the Higgs global fit of 2HDM-I [(a) and (c)] and 2HDM-II [(b) and (d)] at the LHC Run-1. In all plots, we have sample inputs $(M_A,\, M_{12}^2) = (500\text{GeV},\, -(180\text{GeV})^2)$, and the vertical dashed line denotes the alignment limit of the 2HDM.

h^0 (125GeV) at the LHC Run-1.

We combine the significance(Z_0) from both pure leptonic channel $WW^*\gamma\gamma \to \ell\bar{\nu}\bar{\ell}\nu\gamma\gamma$ and semi-leptonic channel $WW^*\gamma\gamma \to q\bar{q}'\ell\nu\gamma\gamma$ at the LHC Run-2 with 300 fb^{-1} integrated luminosity. For this analysis, the relevant mass-parameters of the 2HDM are $(M_H,\, M_A,\, M_{12})$. For demonstration, we will take the sample inputs, $M_H = 300, 400$GeV and $(M_A,\, M_{12}^2) = (500\text{GeV},\, -(180\text{GeV})^2)$. With these, we have two remaining parameters in the 2HDM: the mixing angle α and the VEV ratio $\tan\beta$. In Fig. 9, we impose projected sensitivity of the LHC Run-2 by requiring significance$(Z_0) \geqslant 5$. From this, we derive the red contours in the parameter space of $\cos(\beta-\alpha)-\tan\beta$ plane, for 2HDM-I [plots (a) and (c)] and 2HDM-II [plots (b) and (d)]. The plots (a)-(b) correspond to $M_H = 300$ GeV, and plots (c)-(d) correspond to $M_H = 400$ GeV. This means that the LHC Run-2 with 300 fb^{-1} integrated luminosity can probe the red contour regions in each plot of Fig. 9 with a significance $Z_0 \geqslant 5$. It gives a discovery of a heavier Higgs boson H (with 300 GeV or 400 GeV mass) in the red regions of the 2HDM parameter space.

In Fig. 9, we further present the global fit for the lighter Higgs boson h(125GeV) by using the existing ATLAS and CMS Run-1 data, where the $2\,\sigma$ and $3\,\sigma$ contours of the allowed parameter space are shown by the green and yellow shaded regions, respectively. As we checked, our LHC global fit of the 2HDM is consistent with those in the literature [29]. From this fit, we see that the parameter space favored by the current global fit is around the alignment limit of the 2HDM with $|\cos(\beta-\alpha)| \lesssim 0.55$ for the 2HDM-I and $|\cos(\beta-\alpha)| \lesssim 0.15$ for the 2HDM-II. But, in the 2HDM-II, there is an extra relatively narrow parameter region with $\cos(\beta-\alpha) > 0.15$ and $\tan\beta \gtrsim 2$.

For $M_H = 300$ GeV in the 2HDM-I, the $Z_0 \geqslant 5$ region overlaps a large portion of the parameter space favored by the current LHC global fit. But for the 2HDM-II, the situation is rather different since the overlap becomes much smaller. For the case of $M_H = 400$ GeV, the covered parameter space in the 2HDM-I only has mild changes as compared to that of $M_H = 300$ GeV, this is because the signal rate does not decrease much [cf. Fig. 4(a)], while the kinematical cuts become a bit more efficient. However, for the 2HDM-II, the covered region significantly shrinks for $M_H = 400$ GeV, and the overlap with the global fit region becomes much smaller. This is because the signal rate for the 2HDM-II drops a lot for small $\tan\beta$ region as Higgs mass raises to $M_H = 400$ GeV [cf. Fig. 4(b)].

5. Conclusion

After the LHC discovery of a light Higgs boson $h^0(125\text{GeV})$ at Run-1, searching for new heavier Higgs state(s) becomes a pressing task of the LHC Run-2. Such heavier Higgs state(s) exists in all extended Higgs sectors and can unambiguously point to new physics beyond the standard model (SM).

In this work, we systematically studied the heavier Higgs H^0 production with the new decay channel of di-Higgs bosons, $pp \to H \to hh \to WW^*\gamma\gamma$, at the LHC Run-2. In Sec. 2, we first analyzed the parameter space of the 2HDM type-I and type-II, including the Hhh cubic Higgs coupling (Fig. 1). We computed the decay branching fractions and production cross section of heavier Higgs boson H at the LHC Run-2 over the mass range $M_H = 250 - 600\,\text{GeV}$, as shown in Fig. 2–4. Then, in Sec. 3, we analyzed both the pure leptonic mode $WW^* \to \ell\bar{\nu}\,\bar{\ell}\nu$ and semi-leptonic mode $WW^* \to q\bar{q}'\ell\nu$. This channel has much cleaner backgrounds than the other process $pp \to H \to hh \to b\bar{b}\gamma\gamma$. We computed signal and background events using MadGraph5(MadEvent). We applied Pythia to simulate hadronization of partons and adopted Delphes for detector simulations. We followed the ATLAS procedure for event selections and built kinematical cuts to efficiently suppress the SM backgrounds. We analyzed various kinematical distributions for pure leptonic channel and semi-leptonic channel in Fig. 6 and Figs. 7–8 for three sample H masses $M_H = 300,\ 400,\ 600\,\text{GeV}$, respectively. We presented the signal and background rates of both channels under the kinematical cuts in Table 2–4. In Sec. 4, we combined the significance of pure leptonic and semi-leptonic channels, and analyzed the LHC Run-2 measurement of H as a constraint on the parameter space of the 2HDM-I and 2HDM-2 in Fig. 9. For comparison, we also presented the current Higgs global fit of the LHC Run-1 data in the same plots. Finally, we note that it is hard to detect H with mass above 600 GeV at the LHC (14TeV) runs via di-Higgs production channel. We find it valuable to extend our present LHC study to the future high energy circular colliders $pp(50-100\text{TeV})$ [30], which are expected to further probe the heavier Higgs boson H with mass up to $O(1-5)\text{TeV}$ range via $pp \to H \to hh$ production channel.

Acknowledgments

LCL and HJH are supported in part by National NSF of China (under grants Nos. 11275101 and 11135003) and National Basic Research Program (under grant No. 2010CB833000). CD, YQF and HJZ are supported in part by Thousand Talents Program (under Grant No. Y25155AOU1), and by the CAS Center for Excellence in Particle Physics (CCEPP). HJH acknowledges the support of visiting grants of IAS Princeton and Harvard University during the finalization of this paper.

References

[1] G. Aad *et al.,* [ATLAS Collaboration], Phys. Lett. B 716 (2012) 1 [arXiv:1207.7214 [hep-ex]];
[2] S. Chatrchyan *et al.,* [CMS Collaboration], Phys. Lett. B 716 (2012) 30 [arXiv:1207.7235 [hep-ex]].
[3] For a review, e.g., J. F. Gunion, H. E. Haber, G. L. Kane and S. Dawson, Front. Phys. 80 (2000) 1; and references therein.
[4] For a review, e.g., A. Djouadi, Phys. Rept. 459 (2008) 1 [arXiv:hep-ph/0503173]; and references therein.
[5] For a review, e.g., U. Ellwanger, C. Hugonie, A. M. Teixeira, Phys. Rept. 496 (2010) 1 [arXiv:0910.1785 [hep-ph]]; and references therein.
[6] For recent studies of minimal gauge extensions with two Higgs doublets (including di-Higgs decay channel $H \to hh$), X. F. Wang, C. Du, and H. J. He, Phys. Lett. B 723 (2013) 314 [arXiv:1304.2257]; T. Abe, N. Chen, H. J. He, JHEP 1301 (2013) 082 [arXiv:1207.4103]; and references therein.
[7] For a review, e.g., P. Langacker, Rev. Mod. Phys. 81 (2009) 1199 [arXiv:0801.1345]; and references therein.
[8] R. N. Mohapatra and J. C. Pati, Phys. Rev. D 11 (1975) 566; G. Senjanovic and R. N. Mohapatra, Phys. Rev. D 12 (1975) 1502.
[9] G. C. Branco, P. M. Ferreira, L. Lavoura, M. N. Rebelo, M. Sher, and J. P. Silva, Phys. Rept. 516 (2012) 1 [arXiv:1106.0034 [hep-ph]]; and references therein.
[10] E.g., M. Bowen, Y. Cui and J. D. Wells, JHEP 0703 (2007) 036 [arXiv:hep-ph/0701035]; M. J. Dolan, C. Englert and M. Spannowsky, Phys. Rev. 87 (2012) 055002 [arXiv:1210.8166 [hep-ph]]; N. Craig, J. Galloway and S. Thomas, arXiv:1305.2424 [hep-ph]; B. Dumont, J. F. Gunion, Yun Jiang, and S. Kraml, Phys. Rev. D 90 (2014) 035021 [arXiv:1405.3584 [hep-ph]] and arXiv:1409.4088 [hep-ph]; B. Hespel, D. Lopez-Val, and Eleni Vryonidou, JHEP 1409 (2014) 124 [arXiv:1407.0281 [hep-ph]]; B. Bhattacherjee, A. Chakraborty, and A. Choudhury, arXiv:1504.04308 [hep-ph]; J. Bernon, J. F. Gunion, H. E. Haber, Y. Jiang, and S. Kraml, arXiv:1507.00933 [hep-ph]; and references therein.
[11] The di-Higgs production channel $pp \to hh \to bb\gamma\gamma$ is also important for probing the light Higgs self-interaction h^3, *e.g.,* J. Baglio, A. Djouadi, R. Grober, M. M. Muhlleitner, J. Quevillon, M. Spira, JHEP 1304 (2013) 151 [arXiv:1212.5581 [hep-ph]]; Weiming Yao, arXiv:1308.6302 [hep-ph], in the Proceedings of Snowmass Community Summer Study (CSS 2013), Snowmass on the Mississippi, July 29–August 6, 2013, Minneapolis, MN, USA; A. J. Barr, M. J. Dolan, C. Englert, D. E. Ferreira de Lima, M. Spannowsky, JHEP 1502 (2015) 016 [arXiv:1412.7154 [hep-ph]]; H. J. He, J. Ren, and W. Yao, arXiv:1506.03302 [hep-ph]; and references therein.
[12] G. Aad *et al.* [ATLAS Collaboration], Phys. Rev. Lett. 114 (2015) 081802 [arXiv:1406.5053 [hep-ex]].
[13] CMS Collaboration, CMS-PAS-HIG-13-025 and CMS-PAS-HIG-13-032.
[14] N. Chen, C. Du, Y. Fang, and L. C. Lü, Phys. Rev. D 89 (2014) 115006 [arXiv:1312.7212].
[15] V. Martin-Lozano, J. M. Moreno, C. B. Park, arXiv:1501.03799 [hep-ph].
[16] A. Djouadi, Phys. Rept. 457 (2008) 1 [hep-ph/0503172].
[17] S. Dittmaier *et al.,* [LHC Higgs Cross Section Working Group], arXiv:1101.0593 [hep-ph]; S. Heinemeyer *et al.,* [LHC Higgs Cross Section Working Group], arXiv:1307.1347 [hep-ph]; and references therein.
[18] J. Bernon, J. F. Gunion, H. E. Haber, Y. Jiang, and S. Kraml, arXiv:1507.00933 [hep-ph].
[19] J. Alwall, R. Frederix, S. Frixione, V. Hirschi, F. Maltoni, O. Mattelaer, H. S. Shao and T. Stelzer, *et al.*, JHEP 1407 (2014) 079 [arXiv:1405.0301 [hep-ph]].
[20] A. Alloul, N. D. Christensen, C. Degrande, C. Duhr and B. Fuks, Comput. Phys. Commun. 185 (2014) 2250 [arXiv:1310.1921 [hep-ph]].
[21] T. Sjostrand, S. Mrenna and P. Z. Skands, JHEP 0605 (2006) 026 [arXiv:hep-ph/0603175].

[22] J. de Favereau *et al.,* [DELPHES 3 Collaboration], JHEP 1402 (2014) 057 [arXiv:1307.6346 [hep-ex]].
[23] J. Beringer *et al.,* [Particle Data Group Collaboration], Phys. Rev. D 86 (2012) 010001.
[24] ATLAS Collaboration, ATLAS-CONF-2013-012, March 5, 2013.
[25] G. Aad *et al.,* [ATLAS Collaboration], CERN-OPEN-2008-020 and arXiv:0901.0512 [hep-ex].
[26] J. Adelman, A. Loginov, P. Tipton and J. Vasquez, arXiv:1310.1132 [hep-ex];
S. Dittmaier *et al.* [LHC Higgs Cross Section Working Group Collaboration], arXiv:1101.0593 [hep-ph].
[27] G. Cowan, K. Cranmer, E. Gross, and O. Vitells, Eur. Phys. J. C 71 (2011) 1554 [arXiv:1007.1727 [physics.data-an]].
[28] G. Aad *et al.* [ATLAS Collaboration], arXiv:0901.0512 [hep-ex].
[29] E.g., A. Djouadi and J. Quevillon, JHEP 1310 (2013) 028 [arXiv:1304.1787 [hep-ph]]; C. Y. Chen, S. Dawson and M. Sher, Phys. Rev. D 88 (2013) 015018 [arXiv:1305.1624 [hep-ph]]; B. Dumont, J. F. Gunion, Yun Jiang, and S. Kraml, Phys. Rev. D 90 (2014) 035021 [arXiv:1405.3584 [hep-ph]]; N. Craig, F. D'Eramo, P. Draper, S. Thomas, H. Zhang, JHEP 1506 (2015) 137 [arXiv:1504.04630 [hep-ph]]; and references therein.
[30] FCC collaboration, http://tlep.web.cern.ch and M. Bicer *et al.,* JHEP 1401 (2014) 164 [arXiv:1308.6176 [hep-ex]]; CEPC-SPPC collaboration, http://cepc.ihep.ac.cn